

Real-time Atomic Oxygen Detection Using Transition Metal Oxide Coated Hydrogen-Terminated Diamond Surface

Asaf Bolker¹, Irina Gouzman¹, Moshe Tordjman², Nurit Atar¹, Brian E. Riggs³, Yakov Carmiel¹,
Ronen Verker¹, Eitan Grossman¹, Rafi Kalish², Timothy K. Minton³

¹*Soreq NRC, Space Environment Department, Yavne 81800, Israel*

²*Technion IIT, Solid State Institute, Haifa 3200, Israel*

³ *University of Colorado Boulder, Ann and H.J Smead Aerospace Engineering Sciences, Boulder, CO 80303, USA*

Abstract

Atomic oxygen (AO) is a major cause for the deterioration of spacecraft materials, such as polymers, composites and optical coatings, in low Earth orbit (LEO). AO exposure can degrade thermal, mechanical, or optical system performance, potentially leading to premature mission failure. Future missions, especially for remote sensing, are designed for very low Earth orbit (VLEO) where the variations of thermospheric density and AO flux are more significant than in higher orbits. Therefore, accurate *real-time* assessment of the AO fluence impinging upon spacecraft surfaces becomes a crucial issue for mission success, as well as for improving current thermospheric density models.

We present a compact, solid-state sensor with high sensitivity and fast response to AO. The sensor is based on two semiconductor components that exhibit unique electrical properties when assembled together: hydrogenated diamond substrate and transition-metal oxide (TMO) coating. The Diamond:H-Transitional Metal Oxide AO sensor (DiMO) was characterized using RF plasma-based and laser detonation AO facilities. Tungsten oxide, WO₃, with thickness ranging from 6 nm

to 30 nm was used as TMO coating of choice. The results showed a linear increase in electrical resistance as a function of AO fluence of up to 2×10^{20} O-atoms \cdot cm $^{-2}$, as tested in a laser detonation AO beam facility. The sensitivity of the sensor was found to be tunable, ranging from 10^{-14} to 10^{-15} $\Omega \cdot$ O-atoms $^{-1} \cdot$ cm 2 , and inversely dependent on the coating thickness. This work demonstrates the potential usage of diamond-based devices for VLEO *real-time* AO flux monitoring. Furthermore, compact dimensions and minimal power consumption of the DiMO sensor make it an ideal low-cost solution for the emerging "new-space" era, including nanosatellites applications.

Keywords: Atomic oxygen, Real-time sensing, Low Earth Orbit, Diamond, Metal Oxide Coating

1. Introduction

1.1 Low and very low Earth orbit environment

In low and very low Earth orbit (LEO and VLEO, respectively) altitudes, ranging from 200 to 700 km, the hazardous space environment includes atomic oxygen (AO), UV radiation, ionizing radiation (electrons and protons), ultra-high vacuum, thermal cycles, as well as micrometeoroids and debris. However, AO, formed by UV-induced molecular oxygen dissociation, is considered to be the most hazardous for external satellite surfaces, due to its oxidative and erosive potential. The AO that constitutes the VLEO/LEO environment has a density of 10^7 - 10^{10} cm $^{-3}$ and a relatively low kinetic temperature of 800-1000 K (70-90 meV), depending on altitude and solar activity ¹. Thus, the external surfaces of any spacecraft orbiting at LEO/VLEO altitudes will be exposed to collisions with AO. The typical orbiting speed of a spacecraft in LEO orbit is roughly 8 km \cdot s $^{-1}$, hence the impact energy and flux of the AO on the surface can be as high as ~ 4.5 - 5 eV and 10^{13} - 10^{15} O-atoms \cdot cm $^{-2} \cdot$ s $^{-1}$, respectively ². The AO density, and, consequently, flux depend on the

altitude, the solar activity variation, the orbital inclination and the time of year, thus it is particularly challenging to predict and measure. Advances in spacecraft propulsion systems, such as the development of efficient ion engines, make VLEO accessible for prolonged space missions. Ion engines allow satellites to sustain VLEOs below 400 km for extended periods of time, overcoming the residual atmosphere drag. At these heights the typical AO flux is high (up to 10^{15} O-atoms $\cdot\text{cm}^{-2}\cdot\text{s}^{-1}$)² further exacerbating erosion and oxidation damage compared to higher orbits, making essential the need for monitoring AO in *real-time*.

AO is the major consideration for the protection of the external spacecraft surface since it causes a significant deterioration of polymer-based materials and optical coatings²⁻⁵. Ground and space-borne experiments have shown that prolonged exposure of sensitive spacecraft materials to the LEO environment causes degradation of thermal, mechanical, and optical properties, which can significantly affect mission performance and may even result in premature mission failure^{2,4-7}. In addition, AO is the major contributor to spacecraft drag in LEO and VLEO orbits^{8,9}. Thus, the assessment of the total AO fluence a spacecraft surfaces and subsystems will be exposed to during the mission is crucial for reliability of the whole mission. AO fluence is routinely estimated during the spacecraft design and mission planning stages by applying computer simulation models^{6,10}. These models base their calculations on data observations from atmospheric, weather, and solar activity conditions^{11,12}. However, the lack of AO prediction accuracy might cause considerable additional expenses for external surfaces protection. Therefore, any new data obtained in-flight regarding the dependence of the AO flux on the various parameters, and specifically the dependence on solar activity, will significantly improve quality of the AO density calculations. This will allow accurate forecasting of spacecraft lifetime which leads to a more cost-effective spacecraft design. Furthermore, *real-time* AO monitoring during the mission can be used

to estimate exposure levels of sensitive equipment and manage its protection from AO in case of unexpected high solar activity. Moreover, it can also help to evaluate the atmospheric drag experienced by the spacecraft. Additionally, real time AO measurements may be used as a source of mapping information for solar activity^{13, 14}.

1.2 AO sensing methods

During the past years, several AO sensing methods have been proposed for *real-time* monitoring of the AO fluence¹⁵⁻²². The earliest approach used a space-borne mass spectrometer and was applied extensively in LEO-material interaction experiments performed by NASA^{7, 16, 23, 24}. This method is inherently expensive due to the size and complexity of such devices. Therefore, it was used only in specific experiments where the mass spectrometer versatility was required to examine material interactions with the LEO environment. In these experiments mass spectrometers were used to measure both the AO flux and the surface reaction products.

Another method is based on Quartz Crystal Microbalance (QCM)²⁵. In this method, a quartz crystal is coated with a thin layer of a material with known AO erosion yield (such as KaptonTM, carbon, or silver). The resonant frequency of the quartz crystal depends on its mass, so any reduction in the mass of the material on its surface due to erosion will affect the frequency. Thus, as erosion occurs, the change in frequency is related to the AO flux^{15, 16, 25, 26}. QCMs are relatively small, lightweight, and highly accurate. However, they require a complex and expensive electronic control unit. Additionally, the measurement dynamic range is limited by the thickness of the reference material: once the reference material is fully eroded, the AO flux can no longer be measured.

A more cost-effective method is the use of optical based sensors¹⁷⁻¹⁹. These sensors rely on the measurement of the light intensity passing through a material with known erosion yield

such as KaptonTM or VespelTM in order to detect AO fluence. The detected light intensity can be correlated to the material thickness and, therefore, the AO fluence can be estimated. However, this method is highly affected by light scattering from the etched surface of the exposed material ^{17, 18}. Therefore, in order to increase the accuracy of the measurement, the use of a dedicated light source with a known and constant intensity, in addition to calibration and analysis using different light frequencies, are required ¹⁹.

Another cost-effective method includes the use of actinometers ^{15, 16}. Actinometer is a sensor that changes its electric resistance when its conductive element is exposed to AO. The change in resistance is caused either by erosion of the conductive element, conversion to a non-conducting oxide, or by changes to the material's electronic structure. Knowledge of the element's electrical characteristics and its response to AO exposure provides the means for converting resistance measurements into AO flux/fluence values. Actinometers are usually more compact and require low power to operate compared to other sensing methods ^{16, 22, 27}. Hence, actinometer based sensors are well suited for future “new space” missions involving nano and micro satellites where the size, weight, and power requirements of the sensor are the major limiting factors.

The most used sensing materials to date are silver and carbon, because they have a relatively high reaction rate with AO, they are reasonably inexpensive and are easy to handle. However, much like the QCM method, carbon and silver film actinometers are restricted to missions of limited duration, as the material becomes permanently eroded and/or oxidized by AO. Alternatively, solid-state actinometers that detect changes in electronic properties caused by oxygen interaction processes, other than erosion, have the potential to offer both increased detection sensitivity and higher saturation limits. An actinometer based on graphene was reported ²² and a ZnO-semiconductor-based actinometer has been proposed with regeneration capability,

making repeated measurements of the AO flux ²⁷ possible. However, it reaches saturation at a relatively low AO fluence, and the regeneration process requires heating for a prolonged period of time (15 hours at 80 °C) ²⁷. An actinometer based on the etching of boron-doped diamond has also been proposed and shown to be capable of measuring AO fluences as high as 4×10^{20} O-atoms·cm⁻² ²⁸. Due to the requirement to detect relatively small changes in resistance, the device uses several Wheatstone bridge elements in a specific configuration, which complicates the accurate analysis.

1.3 Transition metal oxide coated hydrogen-terminated diamond

In this work we propose a novel actinometer, based on the electronic properties of a diamond surface coated with a thin layer of transition metal oxide (TMO). This sensor, further denoted as DiMO, has several potential advantages such as long active lifetime, high durability to the space environment, and low power consumption. These advantages make it a highly effective, low-cost solution for real-time AO fluence measurements in LEO and VLEO missions, as well as in ground simulation systems.

DiMO is based on the ability to render the diamond surface as p-type conductive by a process of surface transfer doping (TD) and the ability to affect this process through exposure to oxygen species ²⁹⁻³³. TD is the result of a charge-exchange between a hydrogen terminated diamond (Diamond:H) and a lower energetic surface acceptor. So far, Diamond:H is the only semiconductor for which a true negative electron affinity (NEA) can be achieved ³⁴. The C-H bond on the terminated surface is polarized with a positive charge on the H atom and a negative charge on the C atom. This potential step pulls the vacuum level below the conduction band minimum (CBM) over the distance of the C-H bond length. The maximum NEA measured in hydrogen terminated (100)-oriented diamond by a combination of photoemission and Kelvin probe

experiments was -1.3 eV ³⁵. The NEA induces p-type surface conductivity in air-exposed Diamond:H through an electrochemical charge-exchange with moisture adsorbates on the diamond surface ³⁵. The effect of this charge-exchange on the electronic properties of the diamond surface was thoroughly investigated and the resulting band bending was effectively measured using scanning tunneling microscopy (STM) and scanning tunneling spectroscopy (STS) among other spectroscopic methods ²⁹.

Superior surface conductivity and more stable TD of Diamond:H have been demonstrated with various TMOs, yielded the highest yet reported p-type surface conductivity, and enabled the development of several attractive electronic devices ^{32, 33, 36-38}. TMOs, such as MoO_3 , WO_3 , V_2O_5 , and ReO_3 , are highly interesting semiconductors ($E_g \sim 3\text{ eV}$) due to their deep-lying conduction band and high work function values. Work function is crucial for determining the energetic requirements of transferring electrons to and from a solid until electrodynamic equilibrium is reached. Therefore, TMOs serve as efficient low-lying electron acceptors, and are extensively used for TD of Diamond:H. The TD process in this case involves electrons transferring from the energy levels of diamond valence band maximum (VBM) to the CBM of the TMO coating which is located at a lower energy level, as seen in Figure 1 (a) and (b). This favorable band alignment is due to the combination of the Diamond:H surface's NEA and the large work function of the TMO. The TMO work function can be reduced upon exposure to oxygen and residual moisture, or alternatively, it can increase with increasing TMO layer thickness. This phenomenon is attributed to the tendency of the exposed TMO to alter its O-vacancy concentration, which acts as electronic donors when exposed to oxygen species ³⁹⁻⁴¹.

The reduction in the TMO work function was found to be the cause of a reduction in the diamond p-type conductivity. As the reduction in TMO work function alters the electronic energy

band alignment between the TMO CBM and the VBM of the diamond surface, it initiates a reduction in charge transfer, as seen schematically in Figure 1(c)³¹. Although this is an unwanted effect when designing diamond/TMO electronic devices based on TD³⁶⁻³⁸, DiMO takes advantage of this effect to detect impinging oxygen. The decrease in electrical conductivity of the diamond surface can be correlated with the oxygen fluence during the exposure. Thus, by monitoring changes in conductivity and using a pre-measured calibration function, DiMO-based sensor can be used to deduce the oxygen flux and fluence in real time. In addition, it is possible to regenerate the TMO work function to its pre-exposed value by an annealing process⁴², potentially increasing the AO detection lifetime.

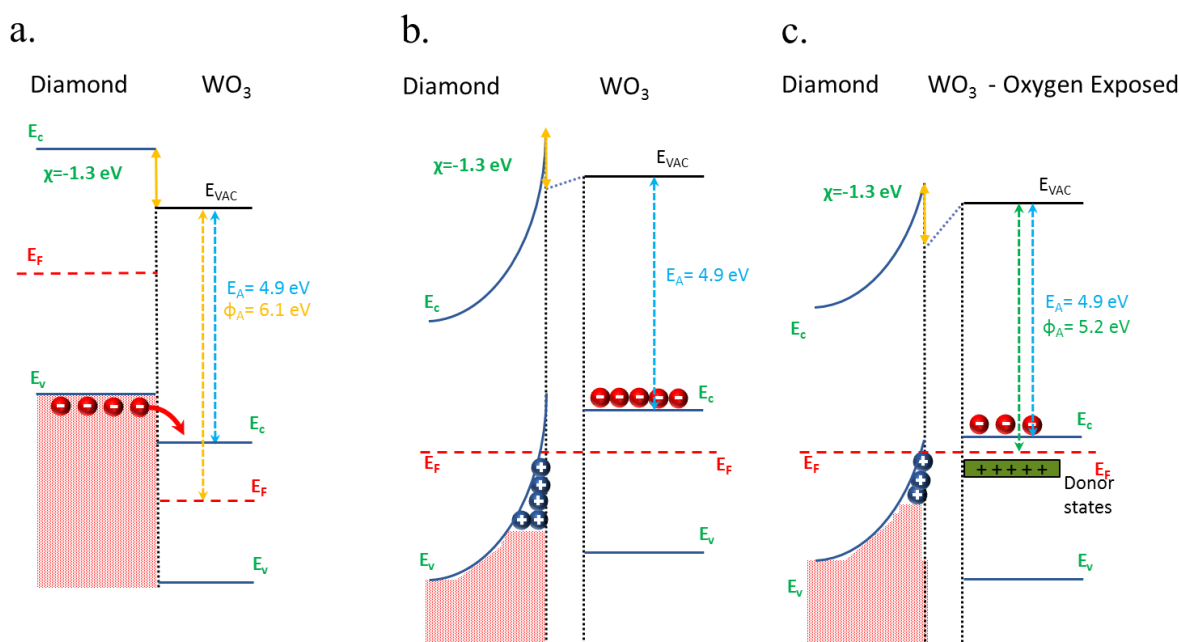


Figure 1: Schematic presentation of energy-level diagram of the surface TD for WO₃-coated diamond (Diamond:H/WO₃): (a) before Diamond:H - WO₃ charge exchange, (b) after equilibrium, and (c) after exposure to oxygen. E_c is the diamond CBM (diamond left, WO₃ right), E_v is the VBM (diamond left, WO₃ right), E_F is the Fermi energy level, E_{VAC} is the vacuum level, E_A is the

WO_3 electron affinity, ϕ_A is the WO_3 work function before (yellow) and after (green) oxygen exposure, χ is the diamond electron affinity (negative due to H surface termination).

In this work, we demonstrate the correlation between DiMO resistance and AO fluence through exposure to (i) ozone, generated by a standard ozone generator, (ii) atomic oxygen, produced by a modified RF oxygen plasma source, and (iii) hyperthermal 5 eV oxygen atoms generated by a laser detonation AO source. Two types of the TMO coating were tested. MoO_3 was chosen for the evaluation tests using ozone exposure due to its well documented role in inducing TD p-type conductivity in diamond, as well as its sensitivity to oxygen exposure^{32, 40}. However, the TMO coating of choice for further studies was tungsten trioxide, WO_3 , which induces a p-type conductive surface layer with electrical properties being superior to those induced by other TMOs³³, enabling higher initial conductivity than the MoO_3 coated samples used for the preliminary ozone exposure. At the first stage, MoO_3 -coated Diamond:H was exposed to ozone in UV ozone generator. The observed changes in the charge carrier concentration allowed to determine the appropriate minimal TMO coating thickness. Following these experiments, DiMO sensors with thicker TMO coating made of WO_3 were exposed to oxygen generated by RF plasma and laser detonation AO source. The assessed AO fluence was compared to the LEO equivalent AO fluence, calculated from the erosion of a KaptonTM reference sample. The sensitivity of the WO_3 -based DiMO sensor to AO exposure as a function of the TMO coating thickness was studied.

2. Materials and Methods

2.1 DiMO sensor fabrication

The DiMO device is composed of a Diamond:H substrate, coated with a thin layer of TMO containing four contacts which enable surface resistance measurement, as depicted schematically

in Figure 2. The fabrication of the DiMO sensor consists of several stages, including hydrogenation of diamond surface, application of TMO coating, and sensor wiring. The diamond substrates are commercially available chemical vapor deposition (CVD) grown type IIa diamonds, purchased from Element SixTM. The substrates are rectangular with dimensions of 3 mm × 3 mm × 0.25 mm and polished surfaces with roughness of $R_q < 30$ nm. They are highly pure and electrically insulating, with a nitrogen concentration lower than 1 ppm and boron concentration lower than 0.05 ppm. In addition, the crystal orientation of the substrate faces is $\langle 100 \rangle$ which was chosen due to its high durability to AO and its ability to achieve high NEA when hydrogen terminated, enabling high p-type conductivity via TD^{35, 43, 44}.

The diamond substrates were hydrogen-terminated by exposure to pure hydrogen plasma in a microwave chemical vapor deposition (MW-CVD) system. The MW-CVD reactor that was used is an Applied Science and Technology (ASTeX) AX5010 reactor. The diamond substrates were exposed to hydrogen plasma induced by a microwave power of 900 W at a temperature of 640 °C and a pressure of 60 Torr for 40 min. Following surface hydrogenation, the diamond substrates were coated with TMO. The coating was performed using thermal evaporation system.

For both MoO₃ and WO₃ coatings, the diamond substrates were heated to 350 °C, *in-situ*, to desorb any moisture and contaminants from the surface. The thickness of MoO₃ was between 1.5 nm to 3.8 nm, while the thickness of WO₃ layer varied between 6 nm to 30 nm. The coated surface of the electrically conductive Diamond:H/WO₃ samples was characterized using scanning electron microscope (SEM) (Zeiss Sigma 300 VP SEM) using a low energy, 1 keV electron beam. SEM was equipped with the energy dispersive X-ray spectroscopy (EDS) detector (Bruker Xflash 1|60). In addition, atomic force microscope (AFM) (Nanoscope IV MultiMode from Veeco) was used to assess surface roughness. The measurements were performed in tapping mode using a

silicon cantilever with a resonance frequency of 79-94 kHz. The AFM image analysis was performed using Gwyddion SPM data visualization and analysis software ⁴⁵.

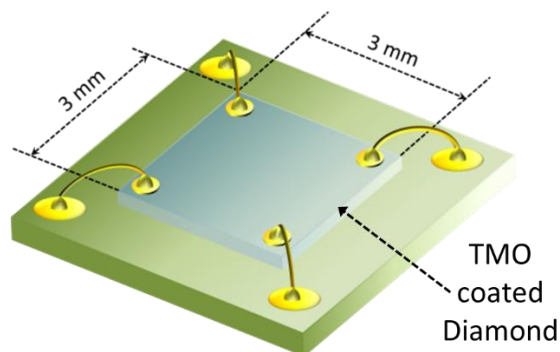


Figure 2: Schematic representation of the DiMO sensor, based on a 3 mm × 3 mm diamond coated with TMO.

Schematic diagram of the coated diamond wiring is shown in Figure 3. The coated DiMO diamond substrates were fixed to a standard printed circuit board (PCB) using a double-sided adhesive carbon tape. Four wire poles (Gore™ AO durable wires) were soldered to the PCB through holes via connectors. These wires were connected to the diamond sample using delicate 45 μm Au coated molybdenum wires attached to the diamond surface in a square configuration using silver paint, see Figure 3(a). In order to prevent damage to the oxygen-sensitive silver contacts, a bismaleimide - based dielectric coating (Designer Molecules, BMI 689) ⁴⁶ was used as a cover layer, as shown in Figure 3 (b) and (c). In addition, a 125 μm-thick Kapton™ mask was used to cover the front of the PCB, leaving a 2 mm-diameter opening to expose the center of the DiMO sensor to the oxygen flux. The final PCB setup can be seen in Figure 3(d).

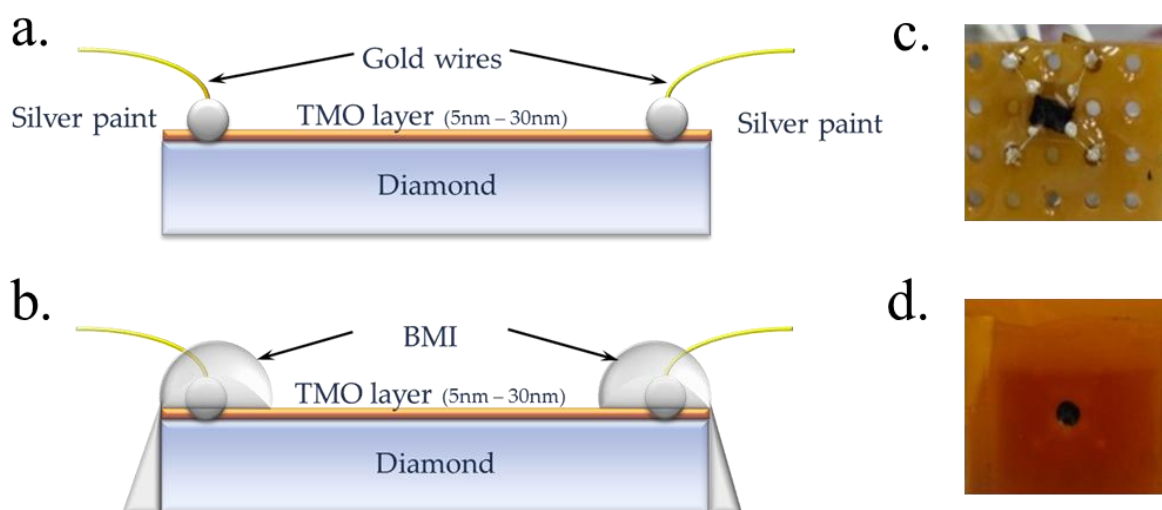


Figure 3: (a) Schematic diagrams of the coated diamond wiring. (b) BMI contact protective coating. (c) Diamond sample electrically connected to four wire poles using Au coated molybdenum wires and silver paint covered with BMI polymer. (d) The entire PCB covered using a Kapton™ mask with a 2 mm diameter opening allowing oxygen exposure of the DiMO surface.

2.2 Ozone exposure

Three MoO₃-coated diamond samples were prepared with a thickness of 1.5 nm, 2.8 nm, and 3.8 nm, respectively. The samples were exposed to ozone for 180 hours using a Novascan Technologies PSDP UV Ozone generator. The surface charge carrier concentration and sheet resistance were measured periodically using a Van der Pauw (VDP) Hall effect system. During the measurements the sample temperature was stabilized at 25 °C using a THMS600 Linkam stage. The current was supplied using a Keithley 220 programmable current source and measured using a Keithley 485 pico-amperemeter. Each of the four contacts was connected to a very high input impedance (TΩ) Keithley 6514 electrometer designed for voltage measurements in high resistivity samples. The voltage difference between each of the two electrometers was measured using a Keithley 2000 multimeter. The current source, electrometers, multimeter and sample contacts were

connected to a Keithley 7001 switch. Hall effect carrier concentration measurements were performed under a magnetic field of 8000 Gauss induced on the sample. All elements in the system were connected to a PC using a General Purpose Interface Bus (GPIB) interface and controlled using the Keithley Testpoint software.

2.3 RF oxygen plasma exposure

The WO₃-based DiMO sensors were exposed to an RF oxygen plasma source, schematically shown in Figure 4, and described in our prior works^{47, 48}. The source is based on a Litmas RPS RF plasma reactor, a Tylan FC-260 mass flow controller valve regulating the oxygen flow, and an Adixon dry vacuum pump. The exposure was performed with an oxygen flow of 5 standard cubic centimeter per minute (SCCM) resulting in a pressure of 2.5×10^{-2} Torr in the exposure chamber. The plasma was ignited by applying RF radiation with a power of 1000 W. The exposure chamber is located down the pumping stream, away from the plasma source. At this position, the sample is exposed to ground state and electronically excited AO species, and to a relatively low current of ions and electrons originated from the plasma⁴⁷. The system is equipped with a temperature-controlled QCM. 6 MHz gold-plated QCM crystals were spin-coated with poly(pyromellitic dianhydride-co-4,4-oxidianiline) (PMDA-ODA) films using a polyamic acid (Pyralin® PI 2545 from HD Microsystems), as described in⁴⁹. Chemical structure of the deposited polyimide (PI) films is similar to that of Kapton™⁴⁹. The LEO equivalent of AO fluence was calculated from the mass loss of a PI layer deposited on the QCM as per ASTM E2089, using the following equation:

$$(1) \quad F = \Delta m / A \rho E$$

where Δm is the mass loss (g), A is the exposed area (cm^2), ρ is the density of PI ($1.42 \text{ g}\cdot\text{cm}^{-3}$), F is the AO fluence ($\text{O-atoms}\cdot\text{cm}^{-2}$), and E is the erosion yield of Kapton H PI ($3\times 10^{-24} \text{ cm}^3\cdot\text{O-atom}^{-1}$)⁵⁰.

The DiMO sensor was mounted close to the QCM, as shown in Figure 4(a). The four-point resistance measurement was performed using a Keithley 2400 Source Measure Unit (SMU). The SMU served as a current source and as a voltmeter connected to the DiMO in a square contact configuration. The resistance measurement was performed by applying a current of $20 \mu\text{A}$ to two of the contacts and by monitoring of voltage drop between the other two. A National Instruments (NI) 9205 16 bit analog-to-digital converter (ADC) was connected in parallel to the SMU in order to provide real-time data acquisition of the voltage measurement during the experiment, as shown in Figure 4(b).

During the experiment both the PI mass loss data and changes in the voltage, induced on DiMO sensor, were measured and logged simultaneously. This was achieved by connecting the QCM Sycon STM-100/MF controller output to an NI 6008 ADC and the DiMO sensor voltage to an NI 9205 ADC. As seen in Figure 4(a), the DiMO sensor was located about 1 cm behind the QCM crystal plane which is perpendicular to the pump flow. Thus, the fluence measured using the QCM can serve as a good estimate of the fluence impinging on the sensor surface. During the experiment, the voltages of the two NI 9205 inputs were logged using a LabVIEW Signal Express software and the QCM voltage signal was converted to thickness values.

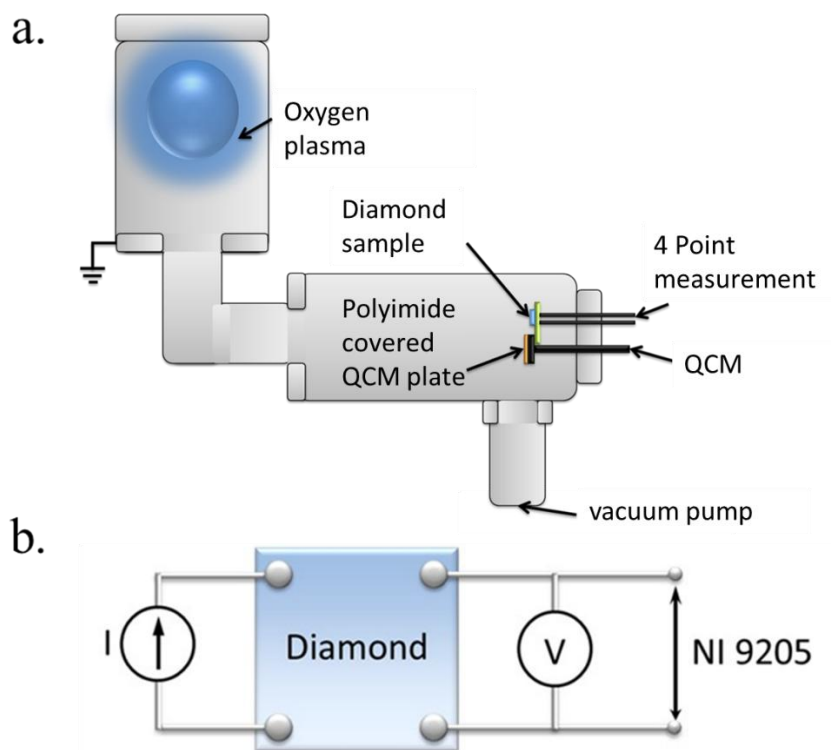


Figure 4: (a) Schematics of the RF oxygen plasma source and the exposure chamber containing the QCM and DiMO sensor. (b) Schematics of the real-time four-point resistance measurement configuration.

2.4 Laser detonation AO facility

Two DiMO sensors were exposed to the well-characterized hyperthermal AO beam in a facility with a laser detonation source, described in detail previously⁵¹⁻⁵³, and shown schematically in Figure 5(a). In this source, a pulsed valve is coupled to an expanding conical nozzle and a pulsed CO₂ TEA laser (Compact 05/50, PaR Systems), operating at ~9 J pulse and 2 Hz repetition rate. The source is capable of producing beams containing 70 – 85% O(³P) atoms, with the rest being molecular oxygen⁵⁴. The characterization of the O/O₂ beam was performed during the exposure by a time-of-flight (TOF) measurements using a custom modified Extrel MAX120 quadrupole mass spectrometer. The mass spectrometer signal is collected for species with m/z of 16 for O, 32

for O₂, and 23 for a background check where no signal is expected. These measurements yield a number density distribution as a function of time $N(t)$. The probability density distributions for velocity and energy, $P(v)$ and $P(E)$, respectively, are determined from the $N(t)$ distributions using the total flight distance, defined from the nozzle throat to the ionizer of the mass spectrometer, and the relations $P(V) \propto t N(t)$ and $P(E) \propto t^2 N(t)$ ⁵⁵. A typical velocity and translational energy distributions of O and O₂, obtained in the present work, are represented in Figure 5(b). The mole ratios of O and O₂ in the hyperthermal beam are approximately 0.74 and 0.26, respectively. The average velocity of the beam is around 7500 m·s⁻¹ and the translational energy of the O atoms is approximately 4.7 eV.

Two DiMO sensors were mounted on the sample holder edge, located at a distance of 40 cm from the nozzle throat, as shown in Figure 6(a). A reference Kapton H sample, covered with a metal mesh screen and mounted in the center position of the sample holder, was used for measurements of the total AO fluence based on Kapton H erosion depth⁵². The DiMO sensor resistance was measured using two Keithley 2000 Digital Multimeter (one for each sample) in a simplified two-point method, as shown schematically in Figure 6(b). The two multimeters were connected to a PC and their data were collected using a dedicated MATLAB script with sampling intervals of 15-60 s.

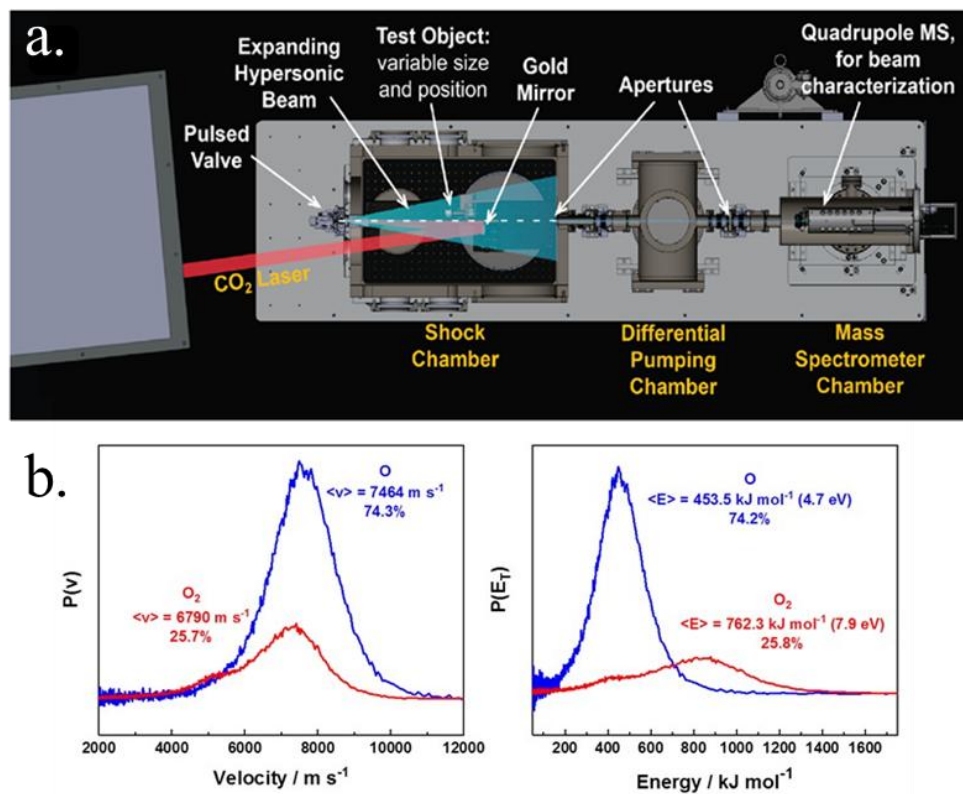


Figure 5: (a) Top view schematic diagram of the AO laser detonation system setup. The CO₂ TEA laser beam is marked in red and the AO beam is marked in blue. A mass spectrometer is used to measure the mole fractions of the constituents in the beam and determine their velocity distributions. (b) The probability density distributions for velocity (left graph) and energy (right graph) of the beam during an exposure experiment.

The LEO equivalent AO fluence was $\sim 2 \times 10^{20} \text{ O-atoms} \cdot \text{cm}^{-2}$, as calculated at the end of the exposure by measuring the erosion depth of Kapton H reference sample with a Dektak3 surface profiler (Veeco Metrology Group, Santa Barbara, CA), using Eq. (1). The beam was stable throughout the experiment, hence the exposure time can be used to calculate the average AO flux. This was done by dividing the total AO fluence by the total exposure time, obtaining LEO equivalent AO flux of $4.4 \times 10^{15} \text{ O-atoms} \cdot \text{cm}^{-2} \cdot \text{s}^{-1}$.

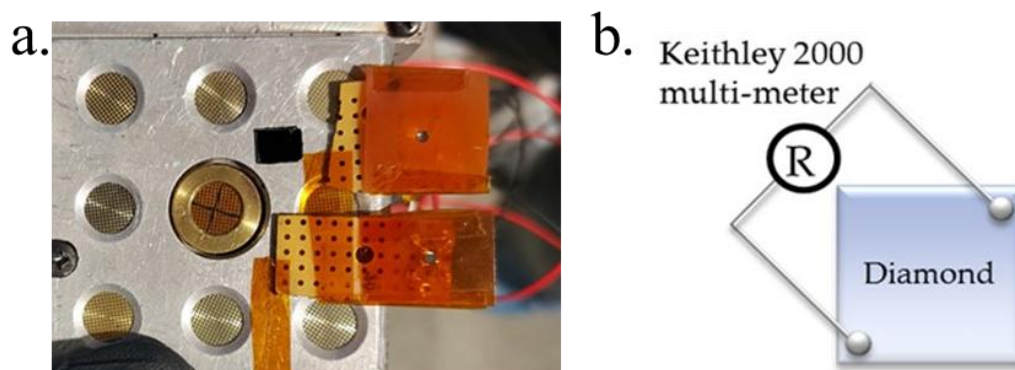


Figure 6: (a) Laser detonation AO source sample holder with two DiMO sensors, mounted on the right edge. A reference Kapton H sample was mounted in the center position, under a metal mesh. (b) Schematic representation of the two-point measurement.

3. Results

3.1. DiMO surface characterization

The key step of the DiMO sensor fabrication is the deposition of a thin, uniform TMO coating on a hydrogenated diamond surface. In the main experiments of the DiMO sensor, we used thermally-evaporated WO_3 coatings with thickness ranging from 6 to 30 nm. Figure 7 shows a SEM image of the surface of a diamond substrate before and after deposition of a 20 nm WO_3 coating. Rectangular pits and triangular features are clearly seen on the hydrogenated diamond surface in Figure 7(a). These features are typical to CVD grown diamond⁵⁶. The fine grains seen in Figure 7(b) are the grains of the WO_3 surface coating. Overall surface roughness increased upon coating, as seen in the images. The presence of the WO_3 coating on the diamond surface was confirmed by EDS (not shown), as indicated by the presence of tungsten (~1.3 at. %), oxygen (~0.5 at. %), along with carbon (98.2 at. %) characteristic X-Ray lines. Further evidence of the coating

uniformity and roughness was obtained using AFM measurements, see Figure 7(c). The RMS roughness, R_q , of the Diamond:H/ WO_3 sample was found to be 6 nm.

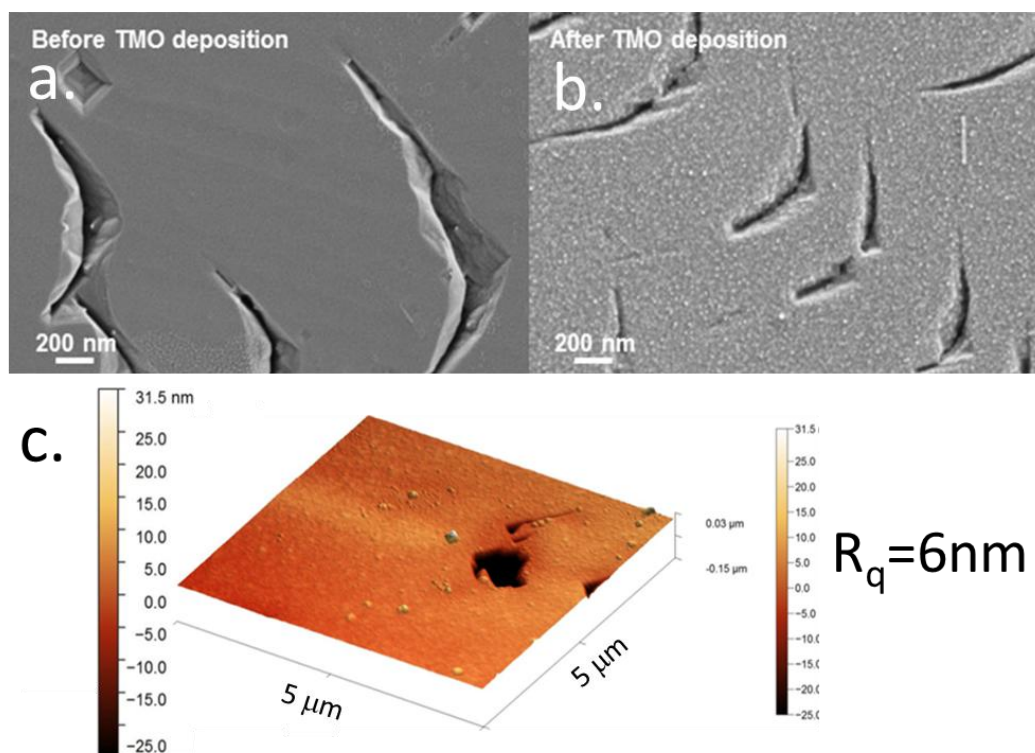


Figure 7: (a) SEM images of the clean Diamond:H surface, and (b) the Diamond:H surface, coated with 20 nm of WO_3 . (c) AFM 3D surface topography image of the Diamond:H surface, coated with 20 nm of WO_3 ($5 \times 5 \mu\text{m}$) showing the RMS roughness of 6 nm.

3.2 Ozone exposure

Diamond:H samples coated with 1.5 nm, 2.8 nm, and 3.8 nm of MoO_3 were exposed to ozone for 180 hours and their charge carrier concentration and sheet conductivity were measured periodically using the VDP measurement technique. The results, depicted in Figure 8, show a significant reduction in carrier concentration and electrical conductance with increasing exposure

for all exposed samples. These results clearly indicate that the reduction in the diamond surface conductivity is the result of reduction in the carrier (hole) concentration at the surface. The reduction in carrier concentration can be associated with reduced TD due to changes of the electronic properties at the TMO – H:Diamond interface induced by oxygen exposure. The 1.5 nm coated sample exhibited the most rapid change in its electronic properties, reducing its carrier concentration and sheet conductance by two orders of magnitude after approximately 50 hours of exposure, while apparently reaching saturation by the end of the exposure. Similarly, the 2.8 nm coated sample showed a rapid reduction in conductivity by one order of magnitude after ~50 hours of exposure, gradually approaching saturation at the end of the 180 hours exposure. In contrast, the 3.8 nm coated sample showed a moderate and roughly linear reduction in electrical conductivity, achieving a reduction by one order of magnitude after 180 hours of exposure. Moreover, unlike the 1.5 nm and 2.8 nm coated samples, the reduction in electrical conductivity of the 3.8 nm coated sample did not approach saturation after 180 hours of exposure. These results correlate well with the observation that oxygen exchange and diffusion in TMOs rapidly reaches a maximum depth of a 1 nm to 2.5 nm, irrelevant of the oxide structure ⁴¹. Therefore, during the exposure of both the 1.5 nm and 2.8 nm MoO₃-coated samples, the entire layer thickness was quickly affected, including the TMO at the diamond interface, resulting in the maximum change in conductivity. However, in the case of the 3.8 nm coated sample, the TMO - diamond interface area was affected gradually, leading to a slower change in its electrical properties, and consequently to slower changes in the TD-induced diamond conductivity. Therefore, a TMO coating thickness greater than 4 nm was chosen for the DiMO sensors fabricated for the AO exposure in the RF plasma and in the laser detonation source facility.

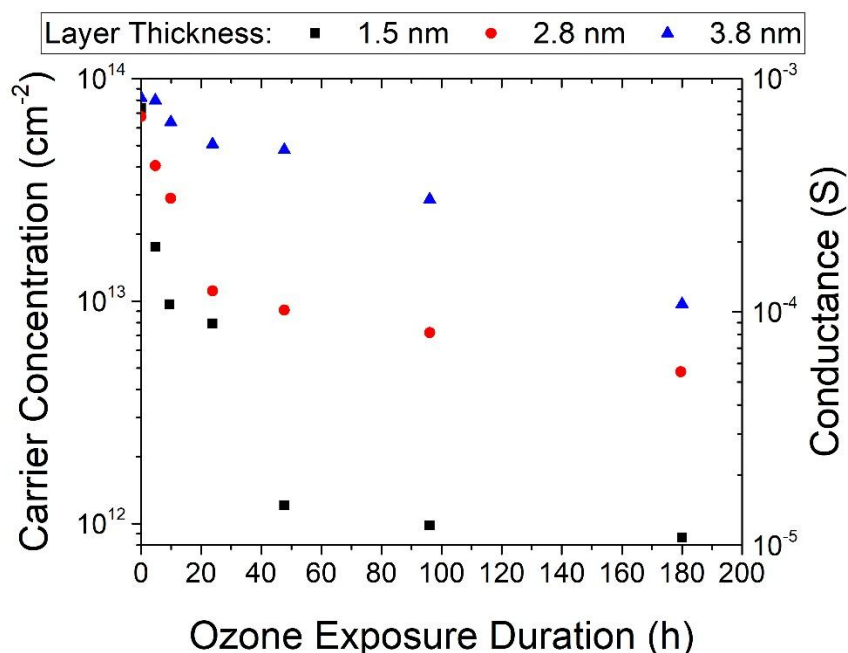


Figure 8: Diamond:H/MoO₃ carrier concentration and surface conductivity as a response to ozone exposure for different thicknesses layers of MoO₃ ranging from 1.5 nm to 3.8 nm.

3.3 DiMO exposure to RF Oxygen plasma

As mentioned above, WO₃ was selected as the choice of TMO due to its ability to induce higher TD surface conductivity compared to MoO₃, potentially increasing DiMO sensitivity and measurement range. Two DiMO sensors, coated with 6 nm and 20 nm thick layers of WO₃, were exposed to RF oxygen plasma in the afterglow region with a reduced concentration of ions and charged oxygen molecular species⁴⁷. Using DiMO sensor electrical resistance data and the AO fluence as measured by the QCM for each exposure experiment, a plot of the diamond resistance as a function of the LEO-equivalent AO fluence was generated for each sample and is depicted in Figure 9. The resistance changes during the exposure of the DiMO sample coated with 6 nm WO₃ are shown in Figure 9(a). These changes can be categorized into three main regimes. First, the

conductivity starts to increase gradually after exposure to 5×10^{17} O-atoms·cm⁻². Then, roughly at a fluence equivalent to 1.9×10^{18} O-atoms·cm⁻² the diamond surface resistance increases linearly with AO fluence. Finally, after exposure to approximately 3.4×10^{18} O-atoms·cm⁻², the diamond resistance reaches saturation. The saturation step was observed in all samples tested in the RF plasma source. It is attributed to the protective BMI coating and Kapton™ cover mask shown in Figure 3(d): the Kapton™ cover mask allows for only a circular area at the center of the diamond surface to be exposed to oxygen species, while the rest of the diamond surface is left unexposed and electrically conductive.

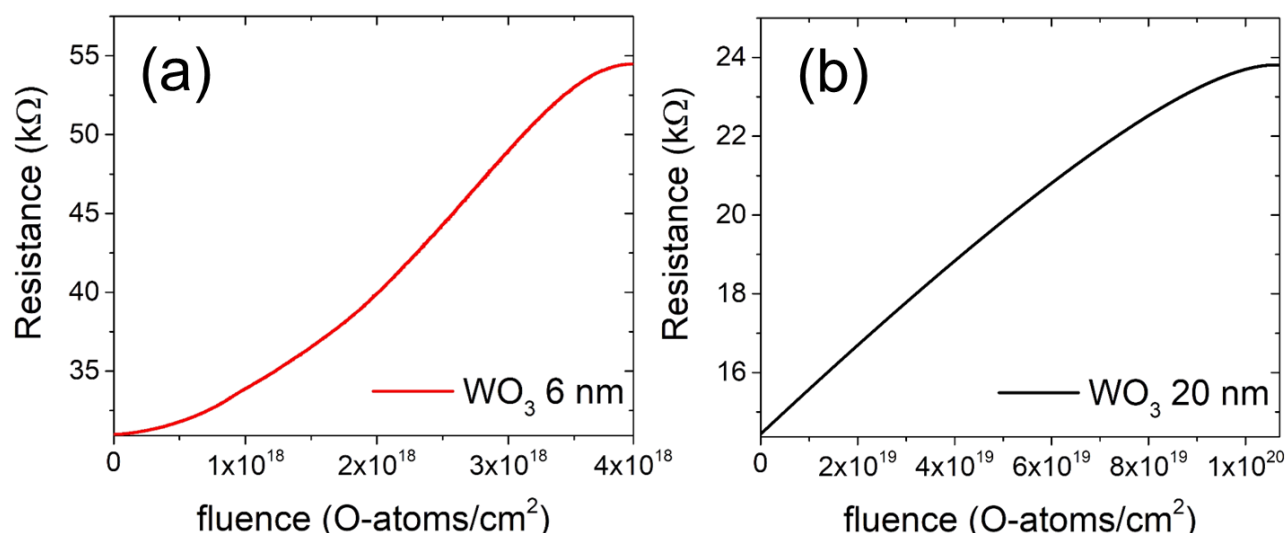


Figure 9: DiMO surface resistance as a function of the accumulated LEO equivalent AO fluence for (a) the 6 nm WO₃-coated Diamond:H, and (b) the 20 nm WO₃-coated Diamond:H.

Figure 9(b) depicts the change in resistance of the 20 nm WO₃-coated DiMO sample as a function of exposure up to AO fluence of 1×10^{20} O-atoms·cm⁻². In this case, we observed the linear dependence of the DiMO resistance on the LEO equivalent AO fluence from the start of the exposure up to saturation at approximately 9×10^{19} O-atoms·cm⁻² while overall resistance was more

than twice lower. This value was one and a half order of magnitude higher than the AO fluence saturation value measured for the 6 nm WO₃-coated DiMO sample.

Using simple linear fitting procedure, a linear calibration function between the WO₃-coated diamond resistance and the LEO equivalent AO fluence was extracted from the linear part of the data gathered during the exposure experiments of both samples:

$$(2) \quad [Fluence (O\text{-}atoms\cdot cm^{-2})] = A \times [Resistance (\Omega)] - B$$

Here parameter *A* represents the AO fluence that will induce a change in resistance of 1 Ω and thus is inversely proportional to the sensitivity of the DiMO surface conductivity to the AO flux. Parameter *A* was found to be equal to 1.2×10^{14} O-atoms·cm⁻²·Ω⁻¹ and 8.7×10^{15} O-atoms·cm⁻²·Ω⁻¹ for the 6 nm and 20 nm WO₃-coated samples, respectively. Parameter *B* represents a baseline AO fluence to be subtracted due to the initial resistance of the unexposed DiMO sensor and the resistance of the contacts. Parameter *B* was found to be equal to 2.7×10^{18} O-atoms·cm⁻² and 1.28×10^{20} O-atoms·cm⁻² for the 6 nm and 20 nm WO₃-coated samples, respectively. These results indicate that the AO fluence saturation level and the calibration parameters *A* and *B* depend on the thickness of the WO₃ coating layer. Most notable is parameter *A*, which is inversely proportional to the sensitivity of the sensor and increases as the WO₃ thickness is increased.

At the next stage, we examined the effect of a variable AO flux on the conductivity of the WO₃-coated diamond surface. For this purpose, another 20 nm WO₃-coated diamond was exposed to RF oxygen plasma while the oxygen gas flow was gradually decreased during the exposure in order to cause the change in the AO flux. The gas flow was changed slowly in the first phase of experiment, but after 5 hours, the gas flow was gradually reduced to 0 SCCM, resulting in a reduction of flux as the oxygen in the system is slowly depleted. The DiMO resistance

measurement was converted into AO fluence using the linear calibration function, according to the Eq. (2), with parameters A and B measured for the similar 20 nm WO_3 coated DiMO in the previous exposure. The fluence detected by DiMO was then compared to the fluence detected by the QCM, as shown in Figure 10(a). As seen in this figure, the DiMO-detected AO fluence is in a good agreement with the AO fluence-detected by the QCM. Furthermore, the AO flux was calculated by differentiating the measured fluence with respect to time for both detectors, DiMO and QCM. AO flux values were plotted on the same graph, as shown in Figure 10(b). The results clearly show that the QCM and DiMO flux measurements are in a good agreement, indicating that the DiMO resistance follows the AO flux change with reasonably good accuracy.

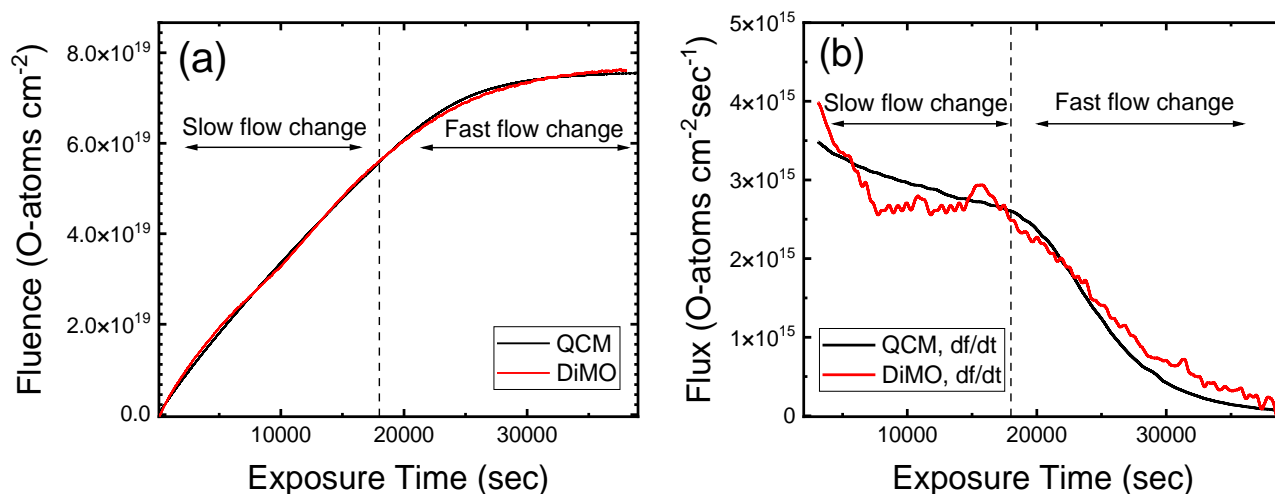


Figure 10: (a) The LEO equivalent AO fluence as measured by QCM (black) and DiMO (red) detectors. (b) The AO flux calculated from the fluence measurements of the QCM (black) and DiMO (red) detectors.

The results of the exposure of WO_3 -coated DiMO sensors to RF oxygen plasma show that it is possible to detect AO flux with good accuracy. However, detection saturation was observed

at a fluence of approximately 9×10^{19} O-atom·cm⁻² using 20 nm WO₃-coated sensor. This value can be considered low for typical LEO missions. Nevertheless, it is well-known that RF oxygen plasma produces significantly more severe exposure conditions compared to the LEO space environment, mostly due to the presence of oxygen ions and charged molecular species^{47, 49}. These charged oxygen species carry a kinetic energy that can reach as high as 278 eV in RF plasma-based system⁵⁷ while the kinetic energy of AO impact on the spacecraft in LEO is substantially lower, about ~4.5 eV². Furthermore, the plasma species are also much more reactive than neutral ground state O(³P) AO in LEO. Therefore, in order to examine the effect of the true hyperthermal AO on the electronic properties of the TMO diamond interface, further exposure experiments were performed using a laser detonation AO source capable of producing hyperthermal O(³P) atoms.

3.4 DiMO exposure in laser detonation AO source

Two DiMO samples, coated by 10 nm and 30 nm thick layers of WO₃, were exposed to a pulsed beam of oxygen atoms with an average translational energy of ~4.7 eV and an average flux of 4.4×10^{15} O-atoms·cm⁻²·s⁻¹ using the laser detonation AO source schematically shown in Figure 5(a). The WO₃ coating thickness in the range of 10 nm to 30 nm was chosen in order to obtain higher saturation limit while preserving good linearity, based on the resistance change of the 20 nm coated DiMO sample during the RF oxygen plasma exposure. As shown in Figure 6, the samples were mounted on the edge of the sample holder to ensure maximum exposure to the AO beam, which expands around the chamber's center axis, as seen in Figure 5(a).

The results of the resistance measurements, taken during the exposure for both the 10 nm and 30 nm WO₃-coated diamond samples, were plotted as a function of the AO fluence, as seen in Figure 11. The measured resistance shows an abrupt increase which settles into a linear response

for the 10 nm sample and a near linear response for the 30 nm coated sample. Neither sample reached saturation up to an accumulated AO fluence of 2×10^{20} O-atoms \cdot cm $^{-2}$. These results indicate a significantly higher DiMO lifetime in similar-to-LEO conditions with hyperthermal AO compared with that obtained in RF plasma-based exposure experiments.

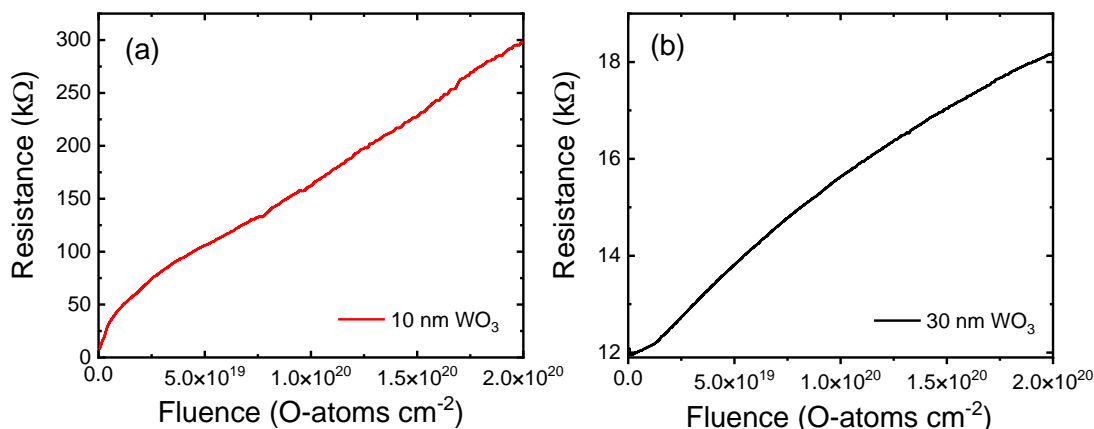


Figure 11: The measured resistance as a function of the accumulated AO fluence for the (a) 10 nm WO₃-coated sample and (b) the 30 nm WO₃-coated sample.

Using the simple linear fit described in Eq. (2), parameter A , which represents the AO fluence that will induce a change in resistance of 1 Ω was found to be 7.7×10^{14} O-atoms \cdot cm $^{-2} \cdot \Omega^{-1}$ and 2.7×10^{16} O-atoms \cdot cm $^{-2} \cdot \Omega^{-1}$ for the 10 nm and 30 nm WO₃-coated diamonds, respectively. Similarly, parameter B for the 10 nm and 30 nm WO₃-coated diamonds was found to be 2.9×10^{19} O-atoms \cdot cm $^{-2}$ and 3.3×10^{20} O-atoms \cdot cm $^{-2}$, respectively.

4. Discussion

The results of DiMO sensor exposure to ozone, and to oxygen atoms produced by RF oxygen plasma and a laser detonation AO source show that it is possible to detect AO flux in *real-time* and with good accuracy while supplying low currents of 20 μ A resulting in a low power

consumption ranging from $1\mu\text{W}$ to $100\mu\text{W}$, depending on DiMO resistance. Furthermore, the obtained results indicate that both the DiMO sensor lifetime (AO fluence saturation level) and detection sensitivity depend strongly on the thickness of the TMO coating layer. Exposure of MoO_3 -coated DiMO to ozone showed that diamond substrates with TMO coating thickness values lower than 2.8 nm reduced their charge carrier concentration and sheet conductance upon exposure by two orders of magnitude after ~ 50 hours, reaching saturation at the end of 180-hour exposure. In contrast, a DiMO coated with 3.8 nm MoO_3 showed a much slower reduction in conductivity and did not reach saturation after the 180-hour exposure. Moreover, DiMO exposure to RF oxygen plasma and to a laser detonation AO source also indicate that the accumulated fluence saturation level and the calibration parameters, A and B , depend on the thickness of the WO_3 coating layer. Parameter A , which is inversely proportional to the sensitivity of diamond surface conductivity to AO, increases with the increased thickness of WO_3 , as shown in Figure 12(a). In other words, the sensitivity of the DiMO sensor to the impinging AO flux is higher as the TMO coating gets thinner, as depicted in Figure 12(b). Therefore, DiMO sensor fabricated using thinner TMO layer is expected to have higher detection sensitivity to AO. On the other hand, RF oxygen plasma exposure results show a fluence detection saturation value of 3.4×10^{18} O-atoms $\cdot\text{cm}^{-2}$ for the 6 nm WO_3 -coated DiMO, roughly 26 times lower than that detected for the 20 nm WO_3 -coated DiMO, 9×10^{19} O-atoms $\cdot\text{cm}^{-2}$. Hence, similarly to the ozone exposure results, DiMO coating thickness is proportional to the detection lifetime.

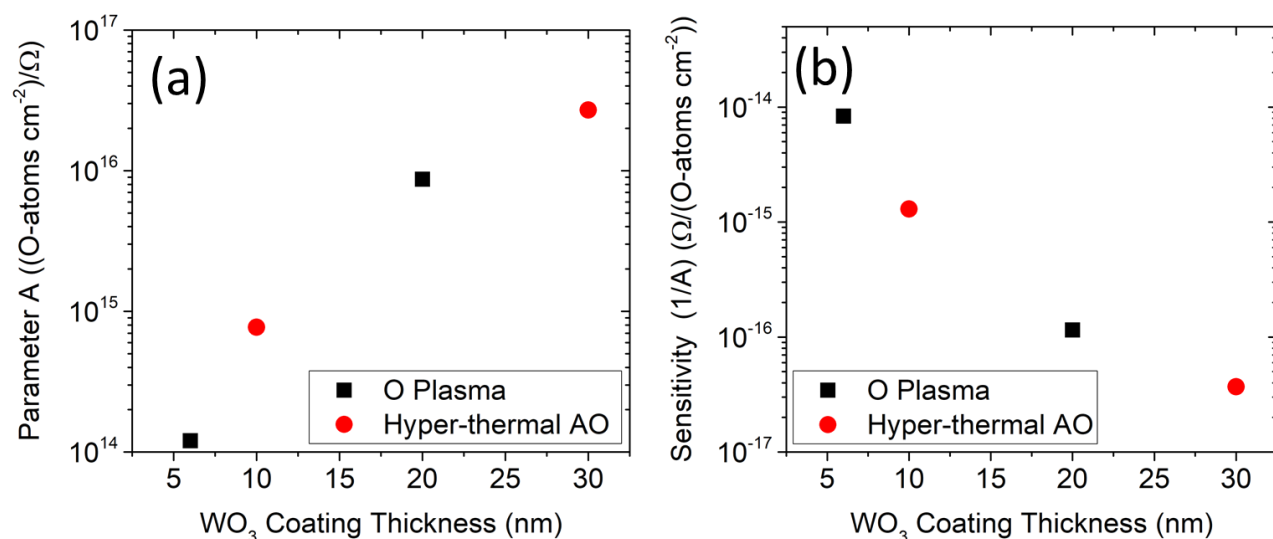


Figure 12: (a) Parameter A as a function of WO_3 coating thickness, as extracted from the RF oxygen plasma exposure experiments (black squares) and the hyperthermal AO exposure experiments (red circles). (b) Plot of the reaction sensitivity (depicted by $1/A$), as a function of WO_3 coating thickness as extracted from the RF oxygen plasma exposure experiments (black squares) and the hyperthermal AO exposure experiments (red circles).

This effect can be related to the fact that the coating thickness determines the rate at which the AO affects the diamond-TMO interface. The diamond conductivity depends on charge transfer from the diamond surface to the WO_3 coating layer³³. Hence, it is mainly affected by the electronic state at the diamond-TMO interface. Therefore, the onset of conductivity change happens when oxygen atoms reach this interface. The interaction of oxygen with various TMOs and its effect on TMO's electronic properties have been studied extensively and shown to involve different processes such as adsorption, oxygen exchange, charge exchange, O_2 formation and desorption, O-vacancy creation, thermal and field induced diffusion, interaction with residual moisture, and more³⁹⁻⁴¹. The oxygen initially affects the top layer of the TMO and then gradually begins to

impact the TMO structure and electronic properties at the interface with the diamond as it propagates through the coating via various diffusion and exchange processes. Once the maximum amounts of AO, O-vacancies, and charge reach the interface layer, the TMO work function — and, consequently, the conductivity of the diamond — will be reduced to their minimum values.

This effect can be seen in the ozone exposure results which correspond well with the reported data on oxygen exchange and diffusion in AO-exposed TMOs, where AO rapidly reaches a depth of 1 nm to 2.5 nm, irrelevant of the oxide structure ⁴¹. Hence, during the exposure of both the 1.5 nm and 2.8 nm MoO₃-coated samples, the entire layer was affected within the exposure time, including the TMO-diamond interface, and the maximum reduction in conductivity was achieved. However, during the exposure of the 3.8 nm coated sample, the TMO-diamond interface area was not entirely affected, allowing for a much slower change to its electrical properties and, therefore, to a slower change in the TD-induced diamond conductivity. Thus, a thinner coating will reduce time to onset of conductivity change, it will make the detector more sensitive to lower AO fluxes and will cause the detector to reach saturation at a lower accumulated fluence. In contrast, use of a thicker TMO layer enables the detection of higher AO fluence, albeit with reduced detection sensitivity.

A rough assessment of the DiMO lifetime as a function of coating thickness can be made assuming a simple diffusion process, e.g. a constant exposure to specific concentration of AO and a diffusion coefficient of $5.5 \times 10^{-22} \text{ m}^2 \cdot \text{s}^{-1}$ for AO in TMO, which is the lowest value of the AO diffusion coefficient measured for MoO₃ and ZrO₂ thin films ⁴¹. The ratio of the AO concentration reaching the TMO-diamond interface area to the concentration of AO at the exposed TMO surface was calculated as a function of time for different TMO coating thicknesses, using the simple solution to diffusion equation in the form of Eq (3).

$$(3) \quad \frac{C_i}{C_0} = \operatorname{erfc} \left(\frac{x_i}{2\sqrt{Dt}} \right)$$

Here C_0 is the constant AO concentration at the TMO outer surface, C_i is the AO concentration at the interface as a function of time, erfc denotes the complimentary error function, x_i is the TMO coating thickness, marking the position of the TMO-diamond interface, t is the time and D is the coefficient of AO in TMO diffusion, taken to be $5.5 \times 10^{-22} \text{ m}^2 \cdot \text{s}^{-1}$. The calculated C_i/C_0 ratio (in percentage) as a function of exposure days can be seen in Figure 13 for coating thickness ranging from 1.5 nm to 30 nm.

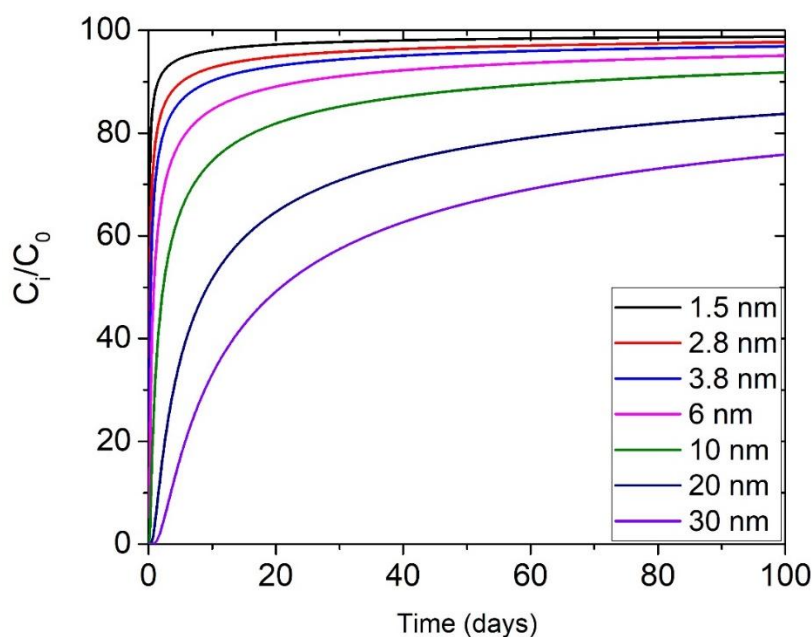


Figure 13: The ratio (%) of the AO concentration at the TMO diamond interface to the AO concentration at the external TMO surface as a function of exposure time (shown for up to 100 days), calculated using Eq. (3) for TMO coating thickness of 1.5 nm (black), 2.8 nm, (red), 3.8 nm (blue), 6 nm (pink), 10 nm (green), 20 nm (dark blue), and 30 nm (purple).

Note that this simple calculation is for thermal AO and does not include changes in O-vacancy concentrations, charge accumulation and various additional processes that can affect electronic properties of the TMO-diamond interface. Nevertheless, the calculation results show the increase in expected DiMO lifetime for thicker TMO coating thicknesses. The plots in Figure 13 show that DiMO devices lifetime increases gradually from less than 10 days of exposure for 1 nm thick coatings to more than 100 days of exposure for 30 nm thick coatings, allowing the detection of higher AO fluences. Thus, the TMO coating thickness can be tailored for specific requirements, trading detection sensitivity for high saturation level required for longer detection lifetime.

In order to use DiMO sensor as an effective AO measurement tool, further research and development are required. As seen by the analysis of the various exposure results, the TMO layer properties are the key for enabling AO detection using DiMO. However, as discussed, this layer is also susceptible to atmospheric O₂ and moisture⁴⁰. The effect of O₂ is expected to be relatively small; the oxygen diffusion coefficient calculated for TMO (ZrO₂) exposed to O₂ was found to be in the range of 10⁻³⁰ m²·s⁻¹, roughly 8 orders of magnitude lower than that found for AO, indicating a much slower degradation process⁵⁸. Nevertheless, an appropriate temporary encapsulation layer should be developed and implemented in order to prevent degradation during storage in a similar manner as to other diamond-based electronic devices³¹. This thin protective layer should be composed of a material that is impermeable to O₂ and moisture, but unlike the encapsulating layer in other diamond electronic device, is sufficiently susceptible to AO erosion. This is required in order to allow the encapsulating layer to be rapidly and completely eroded when exposed to AO in the LEO environment, exposing the TMO layer and allowing AO detection to begin. Several candidate polymers such as BMI, are considered and they will be tested as encapsulating layer in future studies. Moreover, the TD-induced conductivity in diamond is known to be relatively stable

at temperatures below 200 °C³¹; however the temperatures DiMO might be exposed to in LEO and VLEO missions may exceed this value. In order to maintain a constant TD-induced conductivity in diamond at higher temperatures, various thermal stabilization and control methods will be tested. Furthermore, TMOs are capable of regenerating their work function through annealing in air⁴². This ability can potentially increase DiMO detection lifetime and make DiMO detectors serve as fully recyclable devices for AO detection in ground-based systems. The ability of the DiMO sensor to regenerate its original pre-exposed conductivity through annealing will be tested in future studies.

4. Conclusions

A novel AO sensor based on the electronic properties of a diamond surface coated with a thin layer of TMO, denoted as DiMO, is presented. The DiMO sensor is a simple, small in size (a few millimeters), solid-state device with very low power consumption of less than 0.1 mW, as was demonstrated by ground-based AO exposure experiments.

The sensor performance was tested both in RF oxygen plasma and in a laser detonation AO source. A linear correlation between the diamond surface resistance and the AO fluence for a diamond device coated with 6 – 30 nm thick WO₃ was observed. In addition, exposure to hyperthermal AO shows that the device is capable of measuring fluences in excess of 2×10^{20} O-atoms·cm⁻². Furthermore, the electrical resistance sensitivity to AO was found to be tunable in the range of $10^{-14} - 10^{-15}$ Ω·O-atoms⁻¹·cm², inversely dependent on the coating thickness. At the same time, the fluence in which the device resistance reaches saturation was also found to be directly

dependent on TMO coating thickness. Hence, by changing the TMO coating thickness the device could be tailored for specific requirements, trading detection sensitivity for longer sensor lifetime.

The presented work demonstrates the ability of a novel actinometer based on DiMO technology to be used effectively as a tunable AO sensor, capable of measuring a wide range of AO fluxes in real time. With the increased interest in both low-cost “new space” applications and VLEO missions, DiMO AO detectors can serve as an affordable and simple solution in both spacecraft and ground-based AO simulation systems.

References

- (1) U.S. Standard Atmosphere, 1976. **1976**, *NASA-TM-X-74335*.
- (2) Tribble, A. The Space Environment. Princeton University Press, New Jersey: 1995.
- (3) Bedingfield, K. L.; Leach, R. D. Spacecraft system failures and anomalies attributed to the natural space environment. *NASA-RP-1390* **1996**.
- (4) De Rooij, A. Encyclopedia of Aerospace Engineering. John Wiley and Sons Ltd: 2010.
- (5) Grossman, E.; Gouzman, I. Space environment effects on polymers in low earth orbit. *Nuclear Instruments and Methods in Physics Research Section B: Beam Interactions with Materials and Atoms* **2003**, 208, 48-57.
- (6) Bourassa, R. J.; Gillis, J. R. *Atomic oxygen flux and fluence calculation for Long Duration Exposure Facility (LDEF)*; 1991.
- (7) Hilchenbach, M. Space-borne mass spectrometer instrumentation. *International Journal of Mass Spectrometry* **2002**, 215 (1-3), 113-129.

- (8) Ashruf, A. M.; Vineeth, C.; Pant, T. K. On the variability of the atomic oxygen density in the upper atmosphere under different solar activity and geomagnetic conditions and its impacts on satellite drag. *Advances in Space Research* **2024**, *73* (9), 4499-4518. DOI: <https://doi.org/10.1016/j.asr.2024.01.059>.
- (9) Crowley, G.; Pilinski, M.; Azeem, S. Tutorial: The neutral atmosphere and the satellite drag environment. In *Advances in the Astronautical Sciences*, 2012.
- (10) Storz, M. F.; Bowman, B. R.; Branson, M. J. I.; Casali, S. J.; Tobiska, W. K. High accuracy satellite drag model (HASDM). *Advances in Space Research* **2005**, *36* (12), 2497-2505. DOI: <https://doi.org/10.1016/j.asr.2004.02.020>.
- (11) Mahmoud, W. M.; Elfiky, D.; Robaa, S. M.; Elnawawy, M. S.; Yousef, S. M. A standalone prediction model for atomic oxygen and coronal mass ejections. *Astrophysics and Space Science* **2023**, *368* (3), 20. DOI: 10.1007/s10509-023-04170-w.
- (12) Berger, T. E.; Dominique, M.; Lucas, G.; Pilinski, M.; Ray, V.; Sewell, R.; Sutton, E. K.; Thayer, J. P.; Thiemann, E. The Thermosphere Is a Drag: The 2022 Starlink Incident and the Threat of Geomagnetic Storms to Low Earth Orbit Space Operations. *Space Weather* **2023**, *21* (3). DOI: 10.1029/2022SW003330.
- (13) Fuller-Rowell, T. J.; Rees, D. Numerical simulations of the distribution of atomic oxygen and nitric oxide in the thermosphere and upper mesosphere. *Advances in Space Research* **1996**, *18* (9), 255-305. DOI: [https://doi.org/10.1016/0273-1177\(96\)00062-2](https://doi.org/10.1016/0273-1177(96)00062-2).
- (14) Lednyts'kyy, O.; von Savigny, C.; Weber, M. Sensitivity of equatorial atomic oxygen in the MLT region to the 11-year and 27-day solar cycles. *Journal of Atmospheric and Solar-Terrestrial Physics* **2017**, *162*, 136-150. DOI: <https://doi.org/10.1016/j.jastp.2016.11.003>.
- (15) Holmes, B. E. A.; Oiko, V. T. A.; Roberts, P. C. E. A review of satellite-based atomic oxygen sensing methods. *Progress in Aerospace Sciences* **2023**, *137*, 100886. DOI: <https://doi.org/10.1016/j.paerosci.2023.100886>.
- (16) Osborne, J.; Harris, I.; Roberts, G.; Chambers, A. Satellite and rocket-borne atomic oxygen sensor techniques. *Review of Scientific Instruments* **2001**, *72* (11), 4025-4041.

- (17) Verker, R.; Bolker, A.; Carmiel, Y.; Gouzman, I.; Grossman, E.; Minton, T. K.; Remaury, S. Ground testing of an on-orbit atomic oxygen flux and ionizing radiation dose sensor based on material degradation by the space environment. *Acta Astronautica* **2020**, *173*, 333-343. DOI: <https://doi.org/10.1016/j.actaastro.2020.04.065>.
- (18) Verker, R.; Keren, E.; Refaeli, N.; Carmiel, Y.; Bolker, A.; David, D.; Katz, S.; Sagi, E.; Bashi, D.; Finkelstein, I.; Nahum, T.; Haran, A.; Shemesh Sadeh, A.; Ariel, M.; Gouzman, I.; Amrani, O.; Simhony, Y.; Murat, M. Measurements of material erosion in space by atomic oxygen using the on-orbit material degradation detector. *Acta Astronautica* **2023**, *211*, 818-826. DOI: <https://doi.org/10.1016/j.actaastro.2023.07.020>.
- (19) Yukumatsu, K.; Goto, A.; Tsuchiya, Y.; Miyazaki, E.; Kimoto, Y. Evaluation of atomic oxygen fluences by analyzing transmitted light images of polyimide obtained at SLATS/MDM. *Acta Astronautica* **2024**, *214*, 781-789. DOI: <https://doi.org/10.1016/j.actaastro.2023.11.024>.
- (20) Eberhart, M.; Löhle, S.; Steinbeck, A.; Binder, T.; Fasoulas, S. Measurement of atomic oxygen in the middle atmosphere using solid electrolyte sensors and catalytic probes. *Atmospheric Measurement Techniques* **2015**, *8* (9), 3701-3714. DOI: <https://doi.org/10.5194/amt-8-3701-2015> ProQuest Central.
- (21) Zheludkevich, M. L.; Yasakau, K. A.; Gusakov, A. G.; Voropaev, A. G.; Veher, A. A. Two thermodynamics-based approaches to atomic oxygen sensing. *Journal of spacecraft and rockets* **2006**, *43* (2), 426-430. DOI: 10.2514/1.15051.
- (22) Sultana, M.; Herrero, F.; Khazanov, G. Graphene chemical sensors for heliophysics applications. *Radiation effects and defects in solids* **2013**, *168* (10), 805-811. DOI: 10.1080/10420150.2013.831853.
- (23) Hunton, D.; Trzcinski, E.; Cross, J.; Spangler, L.; Hoffbauer, M.; Archuleta, F.; Visentine, J. Mass spectrometers and atomic oxygen. In *Jet Propulsion Lab., Proceedings of the NASA Workshop on Atomic Oxygen Effects*, 1987.
- (24) Visentine, J.; Leger, L. Material interactions with the low earth orbital environment Accurate reaction rate measurements. In *Shuttle Environment and Operations II Conference*, 1985; p 7019.

- (25) Dirri, F.; Palomba, E.; Longobardo, A.; Zampetti, E.; Saggin, B.; Scaccabarozzi, D. A review of quartz crystal microbalances for space applications. *Sensors and Actuators A: Physical* **2019**, *287*, 48-75. DOI: <https://doi.org/10.1016/j.sna.2018.12.035>.
- (26) *QCM Research*. QCM Research, <http://www.qcmresearch.com> (accessed August 2024).
- (27) Osborne, J. J.; Roberts, G. T.; Chambers, A. R.; Gabriel, S. B. Initial results from ground-based testing of an atomic oxygen sensor designed for use in earth orbit. *Review of Scientific Instruments* **1999**, *70* (5), 2500-2506. DOI: 10.1063/1.1149782.
- (28) Haenni, W.; Baumann, H.; Comninellis, C.; Gandini, D.; Niedermann, P.; Perret, A.; Skinner, N. Diamond-sensing microdevices for environmental control and analytical applications. *Diamond and Related Materials* **1998**, *7* (2), 569-574. DOI: [https://doi.org/10.1016/S0925-9635\(97\)00253-7](https://doi.org/10.1016/S0925-9635(97)00253-7).
- (29) Bolker, A.; Saguy, C.; Tordjman, M.; Gan, L.; Kalish, R. Two-dimensional and zero-dimensional quantization of transfer-doped diamond studied by low-temperature scanning tunneling spectroscopy. *Physical Review B* **2011**, *83* (15), 155434.
- (30) Crawford, K. G.; Maini, I.; Macdonald, D. A.; Moran, D. A. J. Surface transfer doping of diamond: A review. *Progress in surface science* **2021**, *96* (1), 100613. DOI: 10.1016/j.progsurf.2021.100613.
- (31) Crawford, K. G.; Qi, D.; McGlynn, J.; Ivanov, T. G.; Shah, P. B.; Weil, J.; Tallaire, A.; Ganin, A. Y.; Moran, D. A. Thermally stable, high performance transfer doping of diamond using transition metal oxides. *Scientific Reports* **2018**, *8* (1), 3342.
- (32) Tordjman, M.; Saguy, C.; Bolker, A.; Kalish, R. Superior surface transfer doping of diamond with MoO₃. *Advanced Materials Interfaces* **2014**, *1* (3), 1300155.
- (33) Tordjman, M.; Weinfeld, K.; Kalish, R. Boosting surface charge-transfer doping efficiency and robustness of diamond with WO₃ and ReO₃. *Applied Physics Letters* **2017**, *111* (11).
- (34) Ristein, J. Surface science of diamond: Familiar and amazing. *Surface Science* **2006**, *600* (18), 3677-3689.
- (35) Maier, F.; Riedel, M.; Mantel, B.; Ristein, J.; Ley, L. Origin of surface conductivity in diamond. *Physical review letters* **2000**, *85* (16), 3472.

- (36) Yin, Z.; Tordjman, M.; Vardi, A.; Kalish, R.; Alamo, J. A. d. A Diamond:H/WO₃ Metal–Oxide–Semiconductor Field-Effect Transistor. *IEEE Electron Device Letters* **2018**, *39* (4), 540-543. DOI: 10.1109/LED.2018.2808463.
- (37) Yin, Z.; Tordjman, M.; Lee, Y.; Vardi, A.; Kalish, R.; del Alamo, J. A. Enhanced transport in transistor by tuning transition-metal oxide electronic states interfaced with diamond. *Science Advances* **2018**, *4* (9), eaau0480. DOI: doi:10.1126/sciadv.aau0480.
- (38) Vardi, A.; Tordjman, M.; Alamo, J. A. d.; Kalish, R. A Diamond:H/MoO₃ MOSFET. *IEEE Electron Device Letters* **2014**, *35* (12), 1320-1322. DOI: 10.1109/LED.2014.2364832.
- (39) Greiner, M. T.; Chai, L.; Helander, M. G.; Tang, W. M.; Lu, Z. H. Transition metal oxide work functions: the influence of cation oxidation state and oxygen vacancies. *Advanced Functional Materials* **2012**, *22* (21), 4557-4568.
- (40) Irfan; Ding, H.; Gao, Y.; Small, C.; Kim, D. Y.; Subbiah, J.; So, F. Energy level evolution of air and oxygen exposed molybdenum trioxide films. *Applied Physics Letters* **2010**, *96* (24), 243307. DOI: 10.1063/1.3454779.
- (41) Stilhano Vilas Boas, C. R.; Sturm, J. M.; Milov, I.; Phadke, P.; Bijkerk, F. Room temperature oxygen exchange and diffusion in nanometer-thick ZrO₂ and MoO₃ films. *Applied Surface Science* **2021**, *550*, 149384. DOI: <https://doi.org/10.1016/j.apsusc.2021.149384>.
- (42) Irfan, I.; Turinske, A. J.; Bao, Z.; Gao, Y. Work function recovery of air exposed molybdenum oxide thin films. *Applied Physics Letters* **2012**, *101* (9), 093305. DOI: 10.1063/1.4748978.
- (43) Shpilman, Z.; Gouzman, I.; Grossman, E.; Shen, L.; Minton, T.; Hoffman, A. Resistance of diamond (100) to hyperthermal atomic oxygen attack. *Applied Physics Letters* **2009**, *95* (17), 174106.
- (44) Shpilman, Z.; Gouzman, I.; Grossman, E.; Shen, L.; Minton, T. K.; Paci, J. T.; Schatz, G. C.; Akhvlediani, R.; Hoffman, A. Oxidation and Etching of CVD Diamond by Thermal and Hyperthermal Atomic Oxygen. *Journal of physical chemistry. C* **2010**, *114* (44), 18996-19003. DOI: 10.1021/jp1073208.

- (45) Gwyddion. *Free SPM (AFM, SNOM/NSOM, STM, MFM) data analysis software*, <http://gwyddion.net/>.
(accessed August 2024).
- (46) Gouzman, I.; Atar, N.; Grossman, E.; Verker, R.; Bolker, A.; Pokrass, M.; Sultan, S.; Sinwani, O.; Wagner, A.; Lück, T.; Seifarth, C. 3D Printing of Bismaleimides: From New Ink Formulation to Printed Thermosetting Polymer Objects. *Advanced materials technologies* **2019**, *4* (10), 1900368. DOI: 10.1002/admt.201900368.
- (47) Shpilman, Z.; Gouzman, I.; Lempert, G.; Grossman, E.; Hoffman, A. rf plasma system as an atomic oxygen exposure facility. *Review of scientific instruments* **2008**, *79* (2), 025106-025106-025106. DOI: 10.1063/1.2885044.
- (48) Gotlib-Vainstein, K.; Gouzman, I.; Girshevitz, O.; Bolker, A.; Atar, N.; Grossman, E.; Sukenik, C. N. Liquid Phase Deposition of a Space-Durable, Antistatic SnO₂ Coating on Kapton. *ACS applied materials & interfaces* **2015**, *7* (6), 3539-3546. DOI: 10.1021/am5072817.
- (49) Grossman, E.; Gouzman, I.; Lempert, G.; Noter, Y.; Lifshitz, Y. Assessment of Atomic-Oxygen Flux in Low-Earth-Orbit Ground Simulation Facilities. *Journal of Spacecraft and Rockets* **2004**, *41* (3), 356-359. DOI: 10.2514/1.10890.
- (50) ASTM-E-2089. *Standard Practices for Ground Laboratory Atomic Oxygen Interaction Evaluation of Materials for Space Applications*; American Society for Testing and Materials, 2002.
- (51) Minton, T. K.; Garton, D. J. Dynamics of atomic-oxygen-induced polymer degradation in low earth orbit. In *Chemical Dynamics in Extreme Environments*, Advanced Series in Physical Chemistry, Vol. Volume 11; WORLD SCIENTIFIC, 2001; pp 420-489.
- (52) Buczala, D. M.; Brunsvold, A. L.; Minton, T. K. Erosion of Kapton H® by Hyperthermal Atomic Oxygen. *Journal of Spacecraft and Rockets* **2006**, *43* (2), 421-425. DOI: 10.2514/1.16402.
- (53) Geistfeld, E. C.; Schwartzentruber, T. E.; Riggs, B. E.; Xu, C.; Gouzman, I.; Minton, T. K. Characterization of the Table-Top Shock Tunnel Facility Using Kapton Erosion Experiments and Direct Simulation Monte Carlo. In *AIAA SCITECH 2023 Forum*, AIAA SciTech Forum, American Institute of Aeronautics and Astronautics, 2023.

- (54) Garton, D. J.; Minton, T. K.; Maiti, B.; Troya, D.; Schatz, G. C. A crossed molecular beams study of the O(3P)+H₂ reaction: Comparison of excitation function with accurate quantum reactive scattering calculations. *J. Chem. Phys.* **2003**, *118* (4), 1585-1588. DOI: 10.1063/1.1539043.
- (55) Giapis, K. P.; Moore, T. A.; Minton, T. K. Hyperthermal neutral beam etching. *Journal of Vacuum Science & Technology A* **1995**, *13* (3), 959-965. DOI: 10.1116/1.579658 (accessed 4/29/2024).
- (56) Tallaire, A.; Kasu, M.; Ueda, K.; Makimoto, T. Origin of growth defects in CVD diamond epitaxial films. *Diamond and Related Materials* **2008**, *17* (1), 60-65. DOI: <https://doi.org/10.1016/j.diamond.2007.10.003>.
- (57) Kearns, D. M.; Gillen, D. R.; Voulot, D.; McCullough, R. W.; Thompson, W. R.; Cosimini, G. J.; Nelson, E.; Chow, P. P.; Klaassen, J. Study of the emission characteristics of a rf plasma source for atomic oxygen: Measurements of atom, ion, and electron fluxes. *Journal of Vacuum Science & Technology A* **2001**, *19* (3), 993-997. DOI: 10.1116/1.1367263 (accessed 8/31/2024).
- (58) Yang, J.; Youssef, M.; Yildiz, B. Oxygen self-diffusion mechanisms in monoclinic ZrO₂ revealed and quantified by density functional theory, random walk analysis, and kinetic Monte Carlo calculations. *Physical Review B* **2018**, *97* (2), 024114. DOI: 10.1103/PhysRevB.97.024114.